

Direct observation of hole carrier density profiles and its light induced manipulation at the surface of Ge

T. Prokscha,^{1,*} K-H. Chow,² Z. Salman,¹ E. Stilp,^{1,3} and A. Suter¹

¹*Laboratory for Muon Spin Spectroscopy, Paul Scherrer Institut, CH-5232 Villigen PSI, Switzerland*

²*Department of Physics, University of Alberta, Edmonton T6G 2E1, Canada*

³*Physics Institute, University of Zurich, 8057 Zurich, Switzerland*

(Dated: April 24, 2022)

We demonstrate that, by using low-energy positive muon (μ^+) spin spectroscopy as a local probe technique, the profiles of free charge carriers can be directly determined in the accumulation/depletion surface regions of p- or n-type Ge wafers. The detection of free holes is accomplished by measuring the effect of the interaction of the free carriers with the μ^+ probe spin on the observable muon spin polarization. By tuning the energy of the low-energy μ^+ between 1 keV and 20 keV the near-surface region between 10 nm and 160 nm is probed. We find hole carrier depletion and electron accumulation in all samples with doping concentrations up to the $10^{17}/\text{cm}^3$ range, which is opposite to the properties of cleaved Ge surfaces. By illumination with light the hole carrier density in the depletion zone can be manipulated in a controlled way. Depending on the used light wavelength λ this change can be persistent ($\lambda = 405, 457$ nm) or non-persistent ($\lambda = 635$ nm) at temperatures < 270 K. This difference is attributed to the different kinetic energies of the photo-electrons. Photo-electrons generated by red light do not have sufficient energy to overcome a potential barrier at the surface to be trapped in empty surface acceptor states. Compared to standard macroscopic transport measurements our contact-less local probe technique offers the possibility of measuring carrier depth profiles and manipulation directly. This new approach may provide important microscopic information on a nanometer scale in semiconductor device studies.

I. INTRODUCTION

The characterization of semiconductor materials and devices is key for understanding and developing semiconductor technologies. Specifically, the changes and the controlled manipulation of charge carrier concentrations at semiconductor interfaces are of fundamental importance for their functionality in devices. With the tremendous growth of the field of semiconductor device physics and the advancement of experimental characterization techniques over the past decades an enormous progress has been achieved, providing new insights and improvements of semiconductor devices [1–3].

Usually, a combination of macroscopic transport measurements and simple modeling are used to determine charge carrier depth profiles and electric field gradients across semiconductor interfaces [1, 2]. Carrier densities can be determined by Hall effect measurements, without depth resolution. The density of dopants can be determined by optical techniques (infrared spectroscopy, photoluminescence, plasma resonance, and free carrier absorption) where depth resolution is also limited. Capacitance-voltage measurements are usually used to gain information about free carrier and impurity profiles in a non-destructive way. These measurements require the manufacture of a Schottky contact, which is not always easy to build. The depth resolution of this technique is limited by the zero-bias space-charge region at the surface, by voltage breakdown at larger depths, and by the Debye limit [2].

A local probe technique, capable of detecting the variation of carrier densities as a function of depth, offers the unique possibility of measuring carrier profiles and their manipulation directly. Here, we employ a beam of polarized low-energy positive muons (LE- μ^+) with tuneable energies between 1 and 20 keV, and implant the μ^+ at variable mean depths between 10 nm and 120 nm in commercial Ge wafers. In semiconductors and insulators the μ^+ stops at an interstitial site, where it can capture zero, one or two electrons to form the hydrogen-like muonium states Mu^+ , Mu^0 , or Mu^- [4, 5]. The interaction of free charge carriers with these muonium states may cause a detectable change of muon spin polarization, which can be observed by measuring the time evolution of the μ^+ polarization in a muon spin rotation (μSR) experiment [4–6]. In this way, the stopped μ^+ may act as “sensor” for free charge carriers. The technique of using LE- μ^+ in depth selective low-energy μSR (LE- μSR) has been recently applied to measure the persistent photo-induced inversion of a Ge surface layer from n- to p-type [7], and the effect of band bending on the activation energy of shallow muonium states close to the surface of commercial CdS and ZnO wafers [8]. These experiments demonstrate the capability of LE- μSR to determine quantitatively i), the charge carrier concentrations in a near-interface region in certain cases (which was in Ref. [7] a photo-induced hole carrier concentration of $\sim 1.5 \times 10^{14} \text{ cm}^{-3}$) and ii), the electric field profile due to band bending at a semiconductor surface/interface [8].

In this paper we significantly advance the methodology to perform depths scans of carrier concentrations of n- and p-type Ge wafers. For the first time we directly explore by means of LE- μSR the hole depletion region

* thomas.prokscha@psi.ch

width at the surface of p-type Ge, and we demonstrate the manipulation of the hole carrier concentration p in the depletion region by using illumination with a blue LED light source or laser (wavelengths $\lambda = 405, 457$ nm), or a red laser ($\lambda = 635$ nm). Whereas after illumination with blue light a persistent increase of hole carrier density $p \gg 10^{14}$ cm $^{-3}$ is observed in the depletion zone, i.e. filling of the depletion region, illumination with red light induces a dynamic charge carrier equilibrium with $p \sim 1 \times 10^{12}$ cm $^{-3}$ at a depth of 20 nm, increasing to $\sim 4 \times 10^{12}$ cm $^{-3}$ at a depth of 120 nm in a p-type Ge wafer with nominal $p \sim 10^{15}$ cm $^{-3}$. At the same time, electron accumulation is found in the surface region without illumination at depths of order 100 nm. Our new method has the potential to provide new insights in charge carrier transport phenomena on a nanometer scale at semiconductor interfaces, relevant for device technology.

II. EFFECT OF FREE CHARGE CARRIERS ON MUON SPIN POLARIZATION

Implantation of a positively charged muon (μ^+) in a semiconductor or insulator normally leads to the formation of a hydrogen-like muonium (Mu) state, where the μ^+ may capture one or two electrons to form the neutral Mu^0 or negatively charged Mu^- state, or it ends up without capturing an electron (Mu^+). Thus, analogous to hydrogen, the three charge states Mu^+ , Mu^0 , and Mu^- can occur, depending on their formation energies and free charge carrier concentrations. The two states Mu^+ and Mu^- , where the μ^+ is not coupled to an unpaired electron, are called *diamagnetic* states, in contrast to the *paramagnetic* state Mu^0 , where the hyperfine coupling with the bound unpaired electron causes an additional magnetic field on the μ^+ . In a transverse-field muon spin rotation experiment (TF- μ^+ SR), where an external magnetic field B is applied perpendicular to the initial muon spin direction, the muon spin in the *diamagnetic* states precesses at the muon Larmor frequency $\nu_\mu = \gamma_\mu/(2\pi) \cdot B$ [$\gamma_\mu/(2\pi) = 135.54$ MHz/T, where γ_μ is the muon gyromagnetic ratio], whereas in Mu^0 , much higher frequencies corresponding to transitions between various hyperfine states are observed [6].

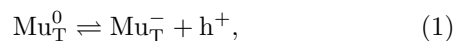
In the group IV or III-V semiconductors with cubic diamond or zinc blende crystal structure, two Mu sites are known: Mu at a bond center (Mu_{BC}), or Mu at the tetrahedral interstitial site (Mu_{T}) [4, 5]. The Mu_{BC} state is usually the donor-like configuration with positive or neutral charge (Mu_{BC}^+ , Mu_{BC}^0), whereas the acceptor like Mu_{T} configuration can be in the neutral or negative charge state (Mu_{T}^0 , Mu_{T}^-). The electron distribution of the Mu_{BC}^0 state is axially anisotropic, with symmetry axis along the $\langle 111 \rangle$ direction. The electron density is centred at the host atoms, and relatively low at the μ^+ site. This explains the small value of the hyperfine coupling A_{hfc} of Mu_{BC}^0 in Ge of the order of 100 MHz, compared to vacuum muonium with $A_{hfc} = 4.46$ GHz. In contrast,

the electron density of Mu_{T}^0 in Ge is much larger and isotropic, with $A_{hfc} = 2.36$ GHz at low temperatures ($T < 40$ K), and linearly decreasing with temperature at $T > 40$ K due to the coupling of Mu_{T} with phonons [9, 10].

The sensitivity of muons to free charge carriers originates from the interaction of the charged/neutral muonium states with these carriers. The interaction may lead to a change of the diamagnetic and paramagnetic fractions, or to a change of muon spin depolarization rates in the presence of cyclic charge-exchange processes, or to phase shifts in the muon spin precession signal if a neutral precursor state transforms into a diamagnetic state [4–6]. The low temperature charge fractions in undoped Ge are about 75% in Mu_{T}^0 , about 10%-20% in Mu_{BC}^0 , and less than 10% in a diamagnetic state [4, 11]. In the presence of free electrons with concentration $n > 10^{17}$ cm $^{-3}$ in doped samples the Mu_{T}^0 acceptor state may capture an electron to form the diamagnetic Mu_{T}^- state, resulting in an increase of the diamagnetic fraction at low temperatures to 30% at $n \sim 2 \times 10^{18}$ cm $^{-3}$, and to 80% at $n \sim 2 \times 10^{19}$ cm $^{-3}$ [12]. Increasing the temperature in Ge leads first to an onset of thermally activated ionization of the Mu_{BC}^0 state at 150 K with an activation energy of about 145 meV [13], where the Mu_{BC}^0 is completely transformed to Mu_{BC}^+ at 200 K [11]. At $T > 200$ K thermally activated ionization of $\text{Mu}_{\text{T}}^0 \rightarrow \text{Mu}_{\text{T}}^-$ sets in with an activation energy of about 170 meV [5, 11, 14], where the diamagnetic fraction reaches 100% close to room temperature.

It is the Mu_{T}^0 state at $T > 200$ K that we use as a sensor for free hole carriers. In the presence of free holes a recombination of a hole h^+ with a Mu_{T}^- state may occur to form again the neutral state. As a consequence charge-exchange cycles between Mu_{T}^0 and Mu_{T}^- are established. These lead to a depolarization of the TF- μ SR precession signal due to fast turning on/off of the hyperfine field in the Mu_{T}^0 state, with a depolarization rate proportional to the hole carrier concentration p [7, 11, 14]. In the absence of holes the depolarization rate of the diamagnetic signal is slow, with rate $\lambda_S < 0.2$ μs^{-1} at $T < 300$ K [7]. In the presence of charge-cycles, a fast component with depolarization rate $\lambda_F > \lambda_S$ appears, where $\lambda_F \propto \Lambda_c$ with Λ_c the hole capture rate.

We developed a Monte-Carlo simulation code [14, 16] for the charge-exchange cycles which allows us, in combination with a calibration measurement on a p-doped wafer with $p = 10^{15}$ cm $^{-3}$, the determination of the hole capture rate Λ_c for a measured muon spin depolarization rate λ_F [14]. The simulation is modeling the cyclic reaction



where the forward reaction (Mu_{T}^0 ionization) is described by an Arrhenius rate process with the temperature dependent ionization rate $\Lambda_i(T) = \Lambda_0 \exp(-E_A/k_B T)$, Λ_0 the attempt frequency, E_A the activation energy, and k_B the Boltzmann constant. The reverse reaction, hole

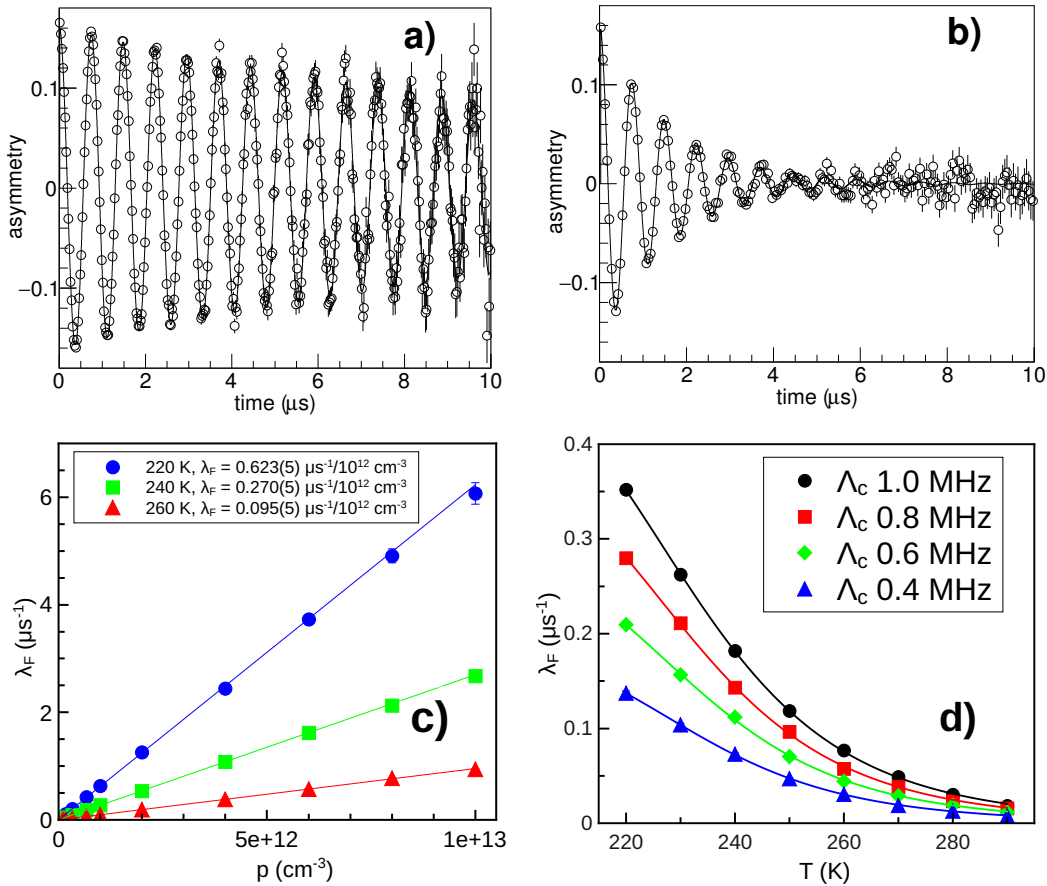


FIG. 1. Simulation data in a transverse field of 10 mT of the charge-cycle of Eq. 1, where we used for the Mu_T^0 ionization $E_A = 154$ meV and $\Lambda_0 = 3.2 \cdot 10^{13}/\text{s}$ (appendix A). a) and b) are for $T = 220$ K, with hole capture rates $\Lambda_c = 0.18$ MHz and 1.8 MHz, corresponding to $p = 10^{11} \text{ cm}^{-3}$ and $p = 10^{12} \text{ cm}^{-3}$ (appendix A), respectively. c) Fast depolarization rate λ_F as a function of hole carrier concentration p and at various temperatures. The solid lines are linear fits to the data, with the slopes given in the legend. d) λ_F as a function of temperature for different hole capture rates Λ_c . The solid lines are fits of Eq. 2.

capture of Mu_T^- , is governed by the hole capture rate $\Lambda_c(T) = p \cdot (v_h \sigma_c^h)(T)$, where we assume a constant p in the temperature range of the experiment, while the temperature dependence of $\Lambda_c(T)$ is absorbed in the product of the hole carrier velocity v_h and the hole capture cross section σ_c^h . It has been shown in the calibration experiment that $v_h \sigma_c^h \propto T^{-2.2(2)}$ (see appendix A), indicating that the temperature dependence of $v_h \sigma_c^h$ is governed by the temperature dependence of the hole mobility ($\propto T^{-2.3}$) [14].

In Ge the assignment of the diamagnetic state at $T > 200$ K has been a matter of debate. It was proposed that the diamagnetic state is Mu_{BC}^+ , which should then also be involved in cyclic charge-exchange reactions [10, 15]. However, the Mu_{BC}^+ state cannot explain the observed suppression of diamagnetic fraction in the presence of holes (Fig. 3 and [11]). The observed temperature dependence of $v_h \sigma_c^h \propto T^{-2.2(2)}$ points towards the involvement of holes in the charge cycles [14], which also favors the Mu_T^- as diamagnetic state. Additionally, if

Mu_{BC}^+ were the relevant diamagnetic state, a large electron concentration of order 10^{17} cm^{-3} should result in a suppression of diamagnetic fraction, or in the appearance of a fast component in this temperature range. However, the investigated sample with $6 \times 10^{17} \text{ cm}^{-3}$ electron doping in Fig. 3 a) does neither show a suppression of diamagnetic fraction, nor a fast component. We take all these observations as strong evidence, that the relevant diamagnetic state is Mu_T^- at $T > 200$ K, and that it is the charge cycle of Eq. 1 determining the muon spin dynamics.

Figure 1 displays the simulation results in an applied transverse field of 10 mT. The increase of the depolarization rate with increasing hole capture rate is obvious from the μSR asymmetry spectra in Fig. 1(a) and (b). Figure 1(c) demonstrates the linear relationship between hole carrier density - which determines the hole capture rate - and the emergent fast depolarization rate λ_F in the presence of charge cycles. Figures 1(c) and (d) show, that for a given p , λ_F decreases with increasing temperature. This is due to the exponentially increasing Mu_T^0 ioniza-

tion rate, which means that the muons spend less and less time in the neutral state, causing less and less dephasing/depolarization of the muon spin during the charge cycles. The solid lines in Fig. 1(d) are fits of the equation

$$\lambda_F = 0.5 \cdot \frac{\Lambda_i \Lambda_c}{\Lambda_i + \Lambda_c} \cdot \frac{\omega_0^2}{\Lambda_i^2 + \omega_0^2(1 + x^2)}, \quad (2)$$

where $\omega_0 = 2\pi \cdot 2150$ MHz is the hyperfine coupling of Mu_T^0 averaged over the temperature range 220 K – 290 K [10], and $x = B/B_0$ with $B_0 = \omega_0/(\gamma_\mu - \gamma_e) = 0.0764$ T is the hyperfine magnetic field at the electron, with gyro-magnetic ratio γ_e . Equation 2 is the expression for $1/T_1$, where $1/T_1$ is the depolarization rate in a longitudinal field (field applied parallel to the initial muon spin direction, LF- μ SR) [10, 17, 18]. Due to the fact that in Ge the TF- μ SR depolarization rate caused by nuclear dipolar fields is small compared to λ_F , the TF- μ SR depolarization rate λ_F can be well approximated by $1/T_1$. This is further supported by the fact that the TF- μ SR simulated data in Fig. 1 d) are very well fitted by Eq. 2. Equation 2 will be used in the analysis of the depth dependent hole carrier profiles under illumination. The temperature dependence of λ_F is mainly determined by the exponential temperature dependence of Λ_i , and to a lesser extent by Λ_c and ω_0 . With increasing temperature, Λ_i is exponentially increasing, causing the decrease of λ_F .

III. EXPERIMENTAL DETAILS

The samples were commercial Ge (100) 2" wafers, 0.5-mm-thick, and nominally undoped, n- or p-type with doping ranges between $4 \times 10^{14} \text{ cm}^{-3}$ and $6 \times 10^{17} \text{ cm}^{-3}$, with relative uncertainties of 10% for n-type and 20% for p-type wafers, as specified by the suppliers (MTI Corporation, Richmond CA, United States, and Crys-tec GmbH, Berlin, Germany). The undoped sample was n-type with a doping of $\sim 5 \times 10^{13} \text{ cm}^{-3}$, as specified by the supplier.

The LE- μ SR experiments were carried out at the low-energy muons (LEM) facility at the μ E4 beam line[19] of the Swiss Muon Source (S μ S, Paul Scherrer Institut, Villigen, Switzerland). A beam of polarized μ^+ with keV energies is generated by moderating a 4-MeV- μ^+ beam, generated by the PSI proton accelerator, in a cryogenic moderator layer of solid Ar/N₂[22–24]. The moderated muons with eV energies are electrostatically accelerated up to 20 keV and transported by electrostatic elements to the sample region. The samples are glued with conductive silver paint on a Ag-coated sample plate made of aluminum, where the final implantation energy E_{imp} is adjusted by applying an electric potential up to ± 12.5 kV to the sample plate. The implantation profiles of muons in Ge with energies between 4 and 18 keV are displayed in Fig. 2. To illuminate the samples, either LEDs or solid state lasers are available [7, 25, 26]. For illumination with blue light we used either a LED source with $\lambda = 405$ nm

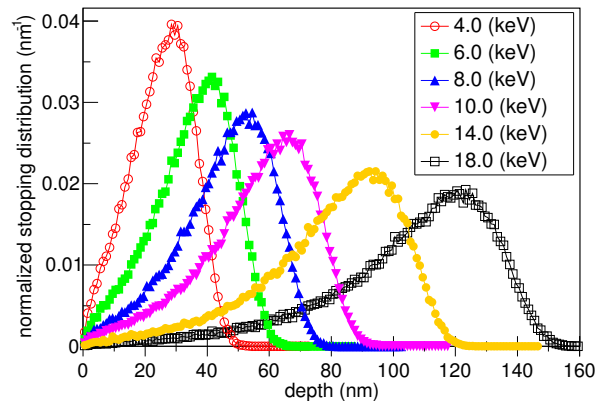


FIG. 2. Calculated muon stopping profiles for various implantation energies in Ge using the program TrimSP[20, 21].

(Bluepoint, Hönle AG, Gräfeling, Germany) or a diode pumped solid state laser with $\lambda = 457$ nm. For red light a diode laser with $\lambda = 635$ nm was used (both lasers from DelMar Photonics Inc San Diego CA, United States). In all cases the maximum light intensity at the sample was 50 - 100 mW/cm².

In addition to the near-surface investigations with LE- μ^+ , the bulk of the Ge wafers was studied at a mean depth of about 300 μm employing the two instruments DOLLY and GPS [27] which use 4-MeV- μ^+ . The original wafers were cut in about 1 cm² pieces to fit into the cryostats of the bulk- μ SR instruments. In all muon experiments the magnetic field was applied parallel to the $\langle 100 \rangle$ direction, and transverse to the initial muon spin direction.

IV. RESULTS

A. Diamagnetic fractions at different depths and doping levels

Figure 3 shows the temperature dependence of the diamagnetic fraction F_D for various Ge samples with different doping levels and at different muon implantation energies, i.e. different mean depths of stopping μ^+ . F_D is defined as the fraction of muons in a diamagnetic state, determined by the fraction of muons precessing at the muons' Larmor frequency. We begin with the description of the bulk μ SR measurements of the undoped and p- and n-type samples [$p \sim 1 \times 10^{15} \text{ cm}^{-3}$ (1p15), $n \sim 6 \times 10^{17} \text{ cm}^{-3}$, (6n17)] in Fig. 3 a). The diamagnetic fraction F_D is $< 20\%$ at $T < 150$ K, and either slowly increasing from 5 K to 150 K for the undoped and 1p15 sample, or nearly constant for the 6n17 sample. Such a weak increase of F_D has been also reported in this temperature range for the samples of Ref. [11] with doping levels $\lesssim 10^{13} \text{ cm}^{-3}$. It can be understood as manifestation of the low-temperature formation of the Mu_T^- state

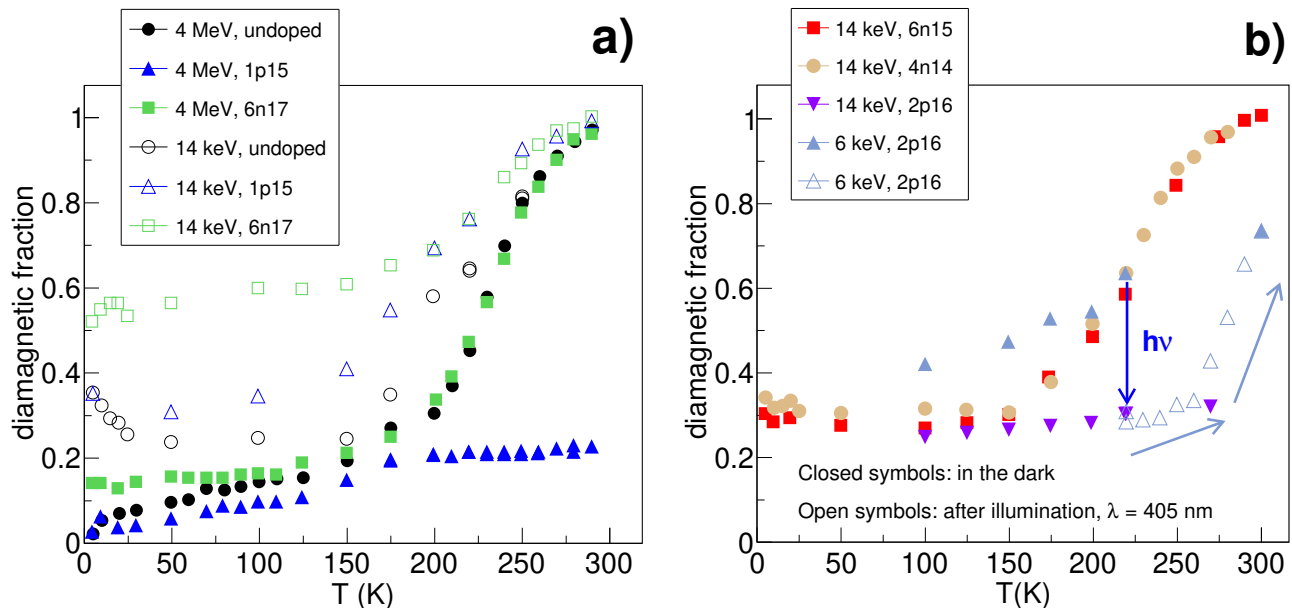


FIG. 3. Diamagnetic fraction as a function of temperature in Ge wafers with different doping levels: nominally undoped n-type, n-type with $n \sim 4 \times 10^{14} \text{ cm}^{-3}$, $\sim 6 \times 10^{15} \text{ cm}^{-3}$, $\sim 6 \times 10^{17} \text{ cm}^{-3}$ (4n14, 6n15, 6n17), and p-type with $p \sim 1 \times 10^{15} \text{ cm}^{-3}$, $\sim 2 \times 10^{16} \text{ cm}^{-3}$ (1p15, 2p16). a) Comparison of LEM data (14 keV, mean depth of 80 nm, 10 mT) with DOLLY and GPS data (4 MeV, $\langle z \rangle \sim 300 \mu\text{m}$, 10 mT and 100 mT). b) LEM data (6 keV and 14 keV, mean depths $\langle z \rangle$ of 35 and 80 nm, respectively) for the 4n14, 6n15 and 2p16 samples. The arrows indicate the evolution of the diamagnetic fraction in the 2p16 sample at 6 keV after illumination with blue light at 220 K. The error bars have about the size of the symbols and were omitted for clearer presentation of the data.

through a transition state, as has been recently proposed as a general feature in the formation of the final muon configuration [28]. In the n-type sample such an increase of diamagnetic fraction is not observed, and might be a consequence of the high electron concentration and/or a modification of the barriers in the transition state due to the doping of the lattice, favoring the formation of Mu_{T}^- already at low temperatures. It is important to note that these subtle effects do not affect the dynamics at $T > 200 \text{ K}$, where the dominant neutral fraction (Mu_{T}^0) becomes thermally ionized. The faster increase of F_D between 150 K and 200 K can be attributed to the thermally activated ionization of Mu_{BC}^0 , which is “completed” at $T \simeq 200 \text{ K}$ [11]. This appears as a flattening of F_D in the 1p15 sample: here the increase of F_D due to the thermally activated formation of Mu_{T}^- at $T > 200 \text{ K}$ is not observable - in contrast to the undoped and 6n17 sample - because the presence of holes drives the reverse reaction in Eq. 1 too quickly.

Implanting the muons much closer to the surface with an energy of 14 keV at a mean depth $\langle z \rangle \simeq 80 \text{ nm}$ reveals considerable differences: i), F_D at $T < 150 \text{ K}$ is significantly larger than in the bulk, ii), the increase of F_D due to thermally activated Mu_{T}^- formation appears to begin at a lower temperature around 150 K, and iii), the most striking feature, we observe the thermally activated formation of Mu_{T}^- in the 1p15 sample. The latter can be explained by the absence of holes at least to a depth of 120 nm, i.e. the presence of a hole depletion layer. This

is supported by the observed weak depolarization rate at 220 K, which is smaller than the expected depolarization rate of $\sim 0.06 \mu\text{s}^{-1}$ for $p \sim 10^{11} \text{ cm}^{-3}$ [Fig. 1 a)], implying $p \lesssim 10^{11} \text{ cm}^{-3}$ in the depletion layer. Additionally, the larger F_D below 100 K indicates an electron accumulation in the near-surface region, with n ranging between $n \sim 10^{18} \text{ cm}^{-3}$ and $\lesssim 10^{19} \text{ cm}^{-3}$ [4, 12]. This means that the 1p15 wafer exhibits a surface layer inversion, where hole depletion and electron accumulation are generated by band bending at the surface. The presence of free electrons in the accumulation region adds to the Mu_{T}^- formation rate due to thermal activation the electron capture rate of the process $\text{Mu}_{\text{T}}^0 + e^- \rightarrow \text{Mu}_{\text{T}}^-$, yielding an enhanced Mu_{T}^- formation rate. This explains the larger F_D values at $T < 150 \text{ K}$, and the lower temperature onset of the increase of F_D , where the thermally activated Mu_{T}^- formation sets in ($T \gtrsim 150 \text{ K}$). The larger value of F_D of the 1p15 sample compared to the undoped sample indicates a higher electron concentration or a larger band bending and accumulation of electrons in the p-type sample. The undoped sample is closer to insulating, implying weaker band bending compared to the p-type sample, i.e. a smaller electron accumulation.

The increase of F_D in the undoped sample at $T < 50 \text{ K}$ can be explained within the thermal spike model [29]. Here, excess heat (due to energy liberated during the stopping process and also as a consequence of stress release to reach the final lattice configuration around the

thermalized Mu^0) may not be quickly enough released to the surrounding lattice due to a reduced thermal conductivity at low temperatures. This may cause thermal ionization of the Mu^0 , increasing the diamagnetic fraction. In the bulk of the sample, this effect obviously does not occur. In contrast, in the surface region with presumably larger lattice distortions [29], causing a reduced thermal conductivity, the thermal spike effect can explain the increase of F_D .

To further support the interpretation of a hole depletion layer, we show in Fig. 3 b) the results of a p-type sample with an order of magnitude larger hole concentration (2p16). We also present for comparison the temperature dependencies of two n-type samples which show similar trends as the undoped sample. In the 2p16 sample at 14 keV ($\langle z \rangle \simeq 80$ nm) the thermally activated formation of Mu_T^- is no longer observed: F_D does not increase at $T > 180$ K, indicating that $p \gg 10^{14} \text{ cm}^{-3}$, or in other words the hole depletion layer is now significantly shifted towards the surface. This is confirmed on lowering E_{imp} to 6 keV ($\langle z \rangle \simeq 35$ nm), where we again observe - as in the case of the 1p15 sample at 14 keV - the thermally activated formation Mu_T^- , which means that the hole depletion layer is still present, but with reduced width. Besides hole depletion the larger value of F_D below 150 K compared to the n-type samples indicates electron accumulation.

B. Hole carrier profile in the depletion region and its manipulation by illumination

As a first attempt to manipulate the depletion region we illuminated the 2p16 sample at 220 K with blue light ($\lambda = 405$ nm) at an intensity of up to 80 mW/cm^2 . Upon light irradiation the value of F_D measured at 220 K at 6 keV implantation energy is comparable to that measured at 14 keV implantation in the dark, indicating that the depletion region is removed, or at least significantly shifted towards the surface. After turning off the light, F_D does not change, demonstrating the persistent change/removal of the depletion layer. This effect has been observed previously [7] and it is attributed to the trapping of photo-generated electrons in empty surface acceptor states, charging the surface negatively and thus pulling holes from the bulk and the photo-generated holes into the depletion region. On warming the sample in the dark, F_D begins to increase at $T \gtrsim 270$ K, where trapped electrons from the surface acceptor states are released and move back into the bulk of the wafer where they recombine with holes, re-establishing the hole depletion zone. The release of the electrons appears as a thermally activated process with an energy barrier of about 1.1 eV [7].

To determine the width of the depletion region in the two p-type samples we measured F_D as a function of E_{imp} between 1 keV and 20 keV at $T = 220$ K, see Fig. 4. In the 1p15 sample only the slowly relaxing component

$F_{D,S}$ is observed, indicating $p \ll 10^{12} \text{ cm}^{-3}$ in the entire energy/depth range accessible by low-energy muons. The solid lines in Fig. 4 a) are from stopping profile simulations (see Appendix B) assuming an increase of p to $\gtrsim 3 \times 10^{11} \text{ cm}^{-3}$ beyond 140 and 150 nm, respectively. In this case, a fast component should appear, leading to a decrease of the slowly relaxing component. No sharp drop of $F_{D,S}$ is observed, excluding an increase of p in this region. This implies, that the depletion width W_D is larger than 160 nm, the maximum range of 20-keV μ^+ in Ge. The observed weak decrease of $F_{D,S}$ can be explained by a slowly increasing activation energy E_A for Mu_T^0 ionization as a function of depth: the presence of an electric field due to the band bending in the depletion zone will result in a reduction of E_A on approaching the surface, increasing the Mu_T^0 ionization rate Λ_i at a fixed temperature, which causes an increase of $F_{D,S}$ [8]. Below 5 keV both samples exhibit $F_{D,S} \simeq 0.8$. In the 2p16 sample at $E_{imp} > 5$ keV, $F_{D,S}$ begins to drop, and the data can be well described by the solid line shown in the figure. This line is calculated assuming $p < 10^{12} \text{ cm}^{-3}$ at depths $z < 45$ nm, and the emergence of holes with $p > 10^{12} \text{ cm}^{-3}$ beyond 45 nm, which implies the appearance of a fast relaxing component $F_{D,F}$. Indeed, we observe this fast component, changing as a function of implantation energy as shown in Fig. 4 b). The data can be best modeled by assuming a depth interval of [45:70] nm, where p is in the range of $p \gtrsim 10^{12} \text{ cm}^{-3}$ and $p < 10^{14} \text{ cm}^{-3}$. A larger $p \gtrsim 10^{14} \text{ cm}^{-3}$ means a too fast depolarization of the μSR signal, causing a loss of the observable $F_{D,F}$. This explains the drop of the sum of both components as a function of E_{imp} : if the μ^+ reach regions with $p \gtrsim 10^{14} \text{ cm}^{-3}$, the fast component can no longer be observed leading to the reduction of $F_{D,F}$ as shown in Fig. 4 b). Figure 4 c) displays p as a function of implantation energy, derived from the measured λ_F by scaling according to the simulation data of Fig. 1 c). It is in the expected range, but the errors are getting large at $E_{imp} > 12$ keV due to the decreasing $F_{D,F}$ and the relatively poor statistics of the data. Thus, no firm conclusions about the carrier profile in the depth range [45:70] nm can be drawn from this plot. Instead, we use simple modeling to calculate carrier profiles and determine the parameters of the model to obtain qualitative agreement with the experimental data. The hole carrier profile $p(z)$ in the depletion region depends on the local band deformation $V(z)$ at depth z as [30]

$$p(z) = N_A \cdot \exp[-V(z)/(k_B T)], \quad (3)$$

where N_A is the bulk acceptor density of the p-type material, and $V(z) = \phi(z) - \phi_B = \phi(z) - \phi(\infty)$, where $\phi(z)$ is the electrostatic potential with its bulk value ϕ_B . Since there is actually not only depletion but inversion at the surface, we can assume that the surface potential ϕ_s determining the band bending significantly exceeds $k_B T$, $|e\phi_s| \gg k_B T$ [30]. In this Schottky space-charge approximation the electrostatic potential decays quadratically

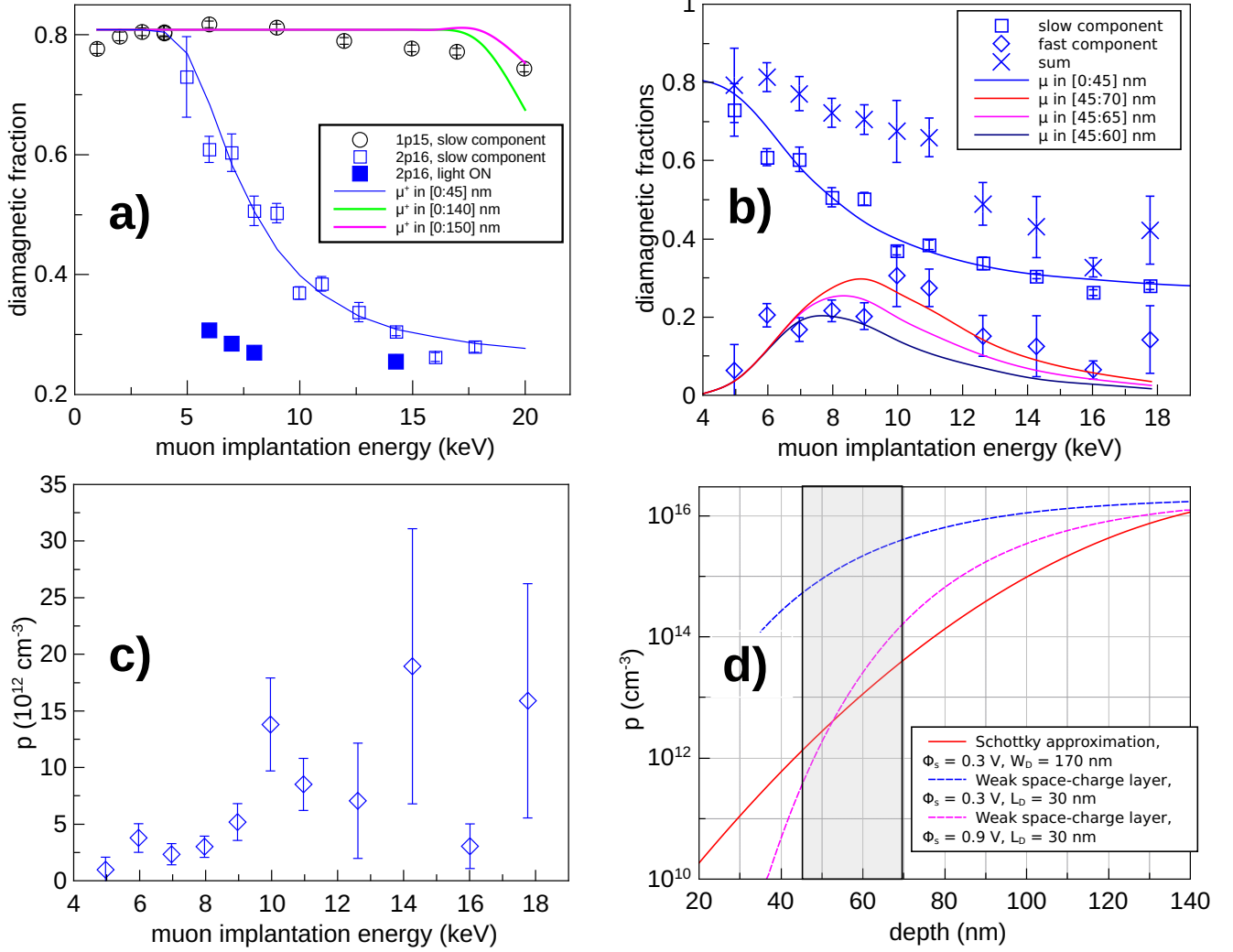


FIG. 4. a) Comparison of energy dependences of the slowly relaxing diamagnetic fraction $F_{D,S}$ in p-type samples at 220 K. Solid squares: F_D after illumination with blue light ($\lambda = 405 \text{ nm}$). The solid lines are simulations (see Appendix B) using the calculated muon stopping profiles and assuming a hole carrier concentration $p \ll 10^{12} \text{ cm}^{-3}$ in the regions indicated in the legend. b) 2p16 sample, where a fast component appears at $E_{imp} \gtrsim 5 \text{ keV}$, implying the presence of holes with $p \gtrsim 3 \times 10^{11} \text{ cm}^{-3}$. The solid lines are simulations giving the fraction of muons stopping in the regions displayed in the legend. c) Hole carrier concentration, calculated from λ_F using the simulation data of Fig. 1 c). d) Calculated $p(z)$ in the Schottky and in the weak space-charge layer approximation using Eq. 3. The shaded area indicates the region where the fast component can be observed by LE- μ SR, which means that p must be in the range $\gtrsim 3 \times 10^{11} \text{ cm}^{-3}$ and $< 10^{14} \text{ cm}^{-3}$ in this region.

from its surface value ϕ_s into the bulk following

$$V(z) = -\frac{eN_A}{2\epsilon\epsilon_0}(z - W_d)^2, 0 \leq z \leq W_d, \quad (4)$$

with a depletion width $W_d = \sqrt{2\epsilon\epsilon_0/(eN_A)\phi_s}$ [1, 2]. Choosing $W_d = 170 \text{ nm}$, i.e. $\phi_s \sim 0.3 \text{ V}$, and inserting in Eq. 3 gives the red curve in Fig. 4 d), resulting in a hole carrier concentration in the shaded area ($z \in [45 : 70] \text{ nm}$) in the range of $10^{12} - 5 \times 10^{13} \text{ cm}^{-3}$, in good agreement with the experimental $p(z)$ in Fig. 4 c). We note, that the Schottly approximation assumes for the free carrier densities $n(z) \approx p(z) \approx 0$, and complete ionization of the acceptors. Due to the electron

accumulation in the hole depletion zone, $n(z) > 0$, thus increasing the negative space charge in this region. For simplicity we assumed in the calibration $n(z) < N_A$, giving a total space charge $N_A + n \simeq N_A$. This seems to be justified by the fact that the bulk N_A values of the two p-type samples seem to be the dominant densities to explain the observed differences in the depletion width estimates below.

For comparison and illustration, we show in Fig. 4 d) the blue curve $p(z)$ in the weak space-charge limit for $\phi_s = 0.3 \text{ V}$ (however, the weak space-charge limit is applicable for $|e\phi_s| < k_B T$, which is not fulfilled here) where

$$V(z) = \phi_s \exp(-z/L_D), \quad (5)$$

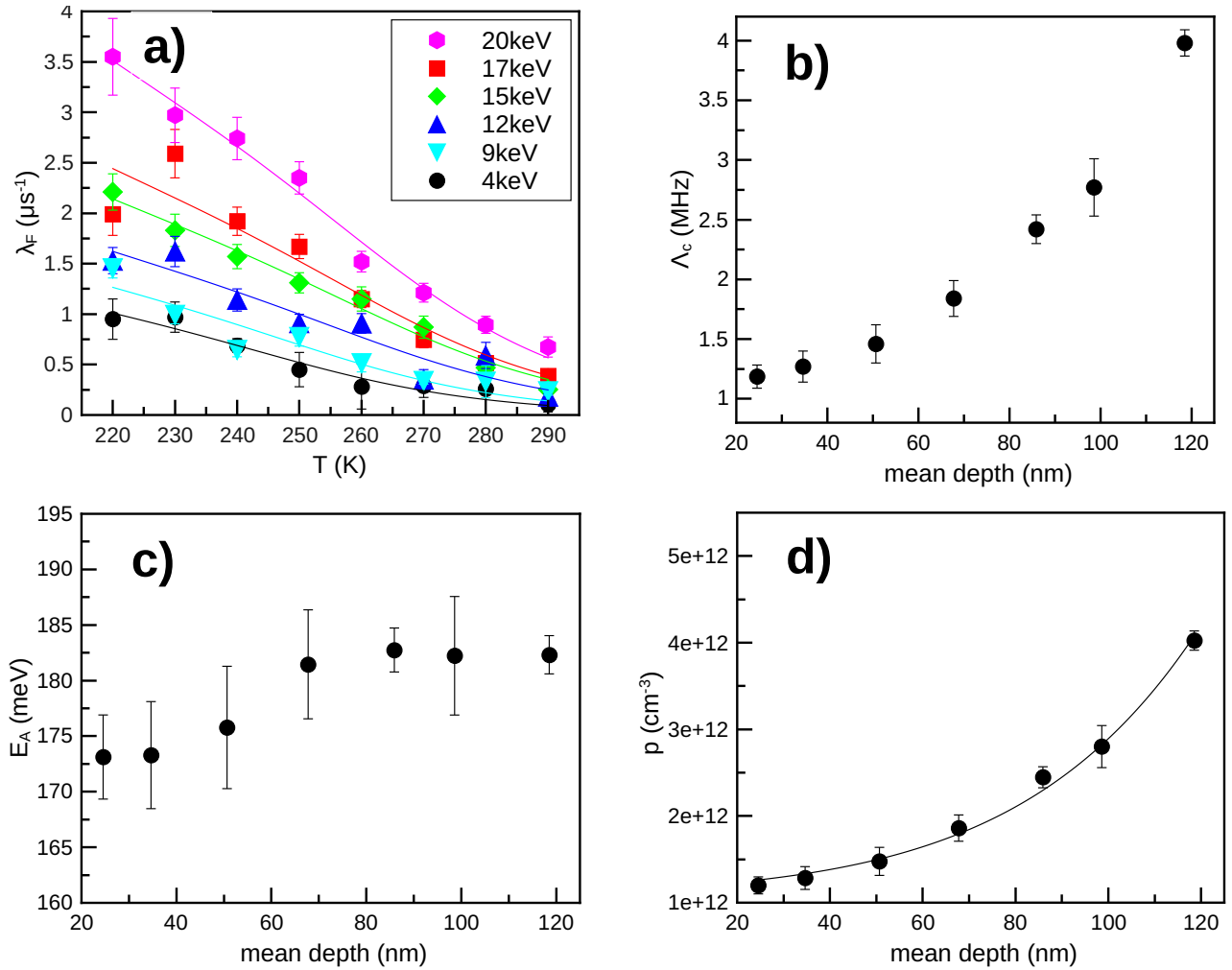


FIG. 5. a) Fast depolarization rate λ_F of the 1p15 sample during illumination with red light ($\lambda = 635$ nm), 10 mT transverse field. The solid lines are fits of Eq. 2 to the data. Fit results for the hole capture rate Λ_c at 290 K, and the Mu_T^0 activation energy E_A are shown in b) and c), respectively. d) Hole carrier concentration p as a function of mean depth, derived from Λ_c . The solid line is a fit of Eq. 3 using the Schottky approximation for $V(z)$, plus a constant offset term p_0 . The fit yields $W_d = 555(2)$ nm and $p_0 = 1.1(1) \times 10^{12} \text{ cm}^{-3}$, where we fixed $N_A = 10^{15} \text{ cm}^{-3}$.

with the Debye length $L_D = \sqrt{\epsilon\epsilon_0 k_B T / (e^2 N_A)} \sim 30$ nm for the 2p16 sample at 220 K. In this case, $p(z)$ would be in the range $5 \times 10^{14} - 5 \times 10^{15} \text{ cm}^{-3}$, in contradiction to the experimental results. In order to bring $p(z)$ into the experimentally observed range one would need to use an even larger $\phi_s = 0.9$ V (magenta curve in Fig. 4 d)), clearly outside the weak space-charge approximation.

The findings of Fig. 4 can be summarized as follows. The data are well described within the Schottky approximation, implying an abrupt change of p from $< 10^{12} \text{ cm}^{-3}$ to $p > 10^{13} \text{ cm}^{-3}$ within about 20 nm commencing at a depth of 45 nm. After illumination with blue light at 220 K, a persistent hole accumulation with $p > 10^{14} \text{ cm}^{-3}$ is established in the depletion region at implantation energies between 6 keV and 14 keV, corresponding to a z range of ~ 10 nm to ~ 120 nm. In the 1p15 sample the width of the depletion layer is esti-

ated to ~ 760 nm, $\sqrt{20}$ times larger than for the 2p16 sample (the width of the depletion layer scales with the square root of the bulk carrier concentration [1]). We estimate the space charge density $N_A \cdot W_d$ for the two samples to $\sim 3.4 \times 10^{11} \text{ cm}^{-2}$ for the 2p16 sample, and $\sim 7.6 \times 10^{10} \text{ cm}^{-2}$ for the 1p15 sample.

Now we turn to the manipulation of p in the wide depletion region of the 1p15 sample by illumination with red light ($\lambda = 635$ nm). Under illumination, again a fast component appears, indicating the presence of photo-generated holes in the depletion zone. However, after turning off the light the fast component disappears and the original slow component fraction $F_{D,S}$ is restored, meaning that the photo-generated holes in the depletion zone immediately disappear by recombination. This suggests, that the photo-electrons generated by red light do not have enough energy to overcome the ~ 1.1 eV barrier

at the surface to reach the empty surface acceptor states. In this case, a dynamic equilibrium of photo-generated holes and electrons is established in the depletion region, and a quick recombination with photo-generated electrons takes place after turning off the light. As shown in Fig. 5 a), the fast component can be tracked in the temperature range from 220 K to 290 K, and from close to the surface at 4 keV ($\langle z \rangle \simeq 25$ nm) to a mean depth of 120 nm at 20 keV. This is different to illumination with blue light, where after an illumination time of 3 min with a laser (instead of the weaker LED source) at $\lambda = 457$ nm and ~ 100 mW/cm², the fast depolarization rate λ_F exceeds values of $60 \mu\text{s}^{-1}$ ($p \gtrsim 10^{14}$ cm⁻³), which is the maximum detectable depolarization rate within the experimental resolution of the LEM apparatus. The fast component can no longer be resolved, and it appears as a “missing” fraction in the μSR spectra, as in Fig. 4 b). In contrast, the dynamic equilibrium photo-generated hole carrier concentration with red light is significantly smaller, with p in the order of 10^{12} cm⁻³, as we will show below.

The increase of λ_F as a function of energy in Fig. 5 a) points towards an increasing hole carrier concentration with increasing depth. For a quantitative analysis we used Eq. 2 to fit the data (solid lines in Fig. 5 a)). In the fits we fixed according to Appendix A i), the exponent of the temperature dependence of Λ_c to -2.2 [$\Lambda_c(T) = \Lambda_c(290\text{K}) \cdot (T/290)^{-2.2}$], ii), the pre-factor Λ_0 in the ionization rate to $3.2 \cdot 10^{13}$ /s, and iii), $\omega_0 = 2\pi \cdot 2150$ MHz, which is the average value of the hyperfine coupling of Mu_T^0 in the temperature range between 220 K and 290 K [10]. The value of Λ_0 is within the range of $1.2 \cdot 10^{13}$ /s and $6.7 \cdot 10^{13}$ /s of pre-factors found in Ref. [10]. The free fit parameters were $\Lambda_c(290\text{K})$ and the activation energy E_A , which are displayed in Figs. 5 b) and c), respectively. From Λ_c the hole carrier concentration $p(\langle z \rangle)$ as a function of mean depth $\langle z \rangle$ is calculated in Fig. 5 d), using the re-analyzed calibration data of Ref. [14] in Appendix A. In doing so we assume that the measured $\lambda_F(E_{imp})$ at implantation energy E_{imp} equals $\lambda_F(\langle z \rangle)$ at the corresponding mean depth. The justification for the validity of this assumption is discussed in Appendix C.

Figure 5 c) indicates a change of E_A by about 10 meV under illumination between the near-surface region and a depth of about 80 nm, where it reaches its bulk value. This indicates a rather weak band bending under illumination with an electric field < 0.5 mV/nm, where E_A is reduced by < 10 meV [8]. According to Fig. 5 d), the electric field is becoming too weak to change E_A within errors in regions where $p \gtrsim 2 \times 10^{12}$ cm⁻³. These electric field values are confirmed by fitting Eq. 3 in the Schottky approximation to the data in Fig. 5 d). In order to obtain a good fit we added a constant offset term p_0 to Eq. 3, where we attribute the appearance of p_0 to the non-equilibrium situation under illumination. The fit yields a depletion width $W_d \sim 555$ nm, which is significantly smaller than the estimated $W_d \sim 760$ nm for the dark sample. A lowering of W_d under illumination

is expected due to the reduction of band bending by the partial compensation of the surface charge by the photo-generated charge carriers. Using the reduced value of W_d in Eq. 4 gives an electric field of ~ 0.5 mV/nm at a depth of 80 nm, in good agreement with the expected value estimated above.

V. DISCUSSION

By means of low-energy μSR we determined directly the free charge carrier profile $p(z)$ at the surface of a semiconductor. Knowing $p(z)$, the electrostatic potential $\phi(z)$ can be calculated using Poisson’s equation. A direct experimental determination of the bending of $\phi(z)$ at the surface is possible by photoemission spectroscopy. However, this method is limited to the first few nanometers at the surface, i.e. to high bulk doping levels $\gtrsim 10^{19}$ cm⁻³, because only in this case the depletion range is comparable to the photo-electron escape depth [31]. We note, that $\phi(z)$ can be also determined directly by LE- μSR in cases, where a change of Mu^0 activation energies is observable [8]. In contrast to photoemission spectroscopy the sensitivity of LE- μSR to free hole carrier concentrations is orders of magnitude larger in Ge: $p(z)$ as low as $\sim 10^{11}$ cm⁻³ can be detected by LE- μSR over a hundred times longer length scale of about 200 nm with a resolution of a few nanometers. This resolution exceeds significantly the capabilities of capacitance-voltage techniques, where due to the Debye-length limitation it is not possible to profile closer than about $1L_D$ to the surface [2], which is ~ 30 nm in the 2p16 sample, and ~ 130 nm in the 1p15 sample.

The high sensitivity to holes in the $\text{Mu}_T^- + h \rightarrow \text{Mu}_T^0$ reaction is due to the large hole capture cross section $\sigma_c^h \sim 10^{-13}$ cm² of Mu_T^- , where we estimate σ_c^h using the relation $\Lambda_c = p \cdot v_h \cdot \sigma_c^h$ with $\Lambda_c = 0.15$ MHz (corresponding to $p \sim 10^{11}$ cm⁻³) as a lower detection threshold [Fig. 1 a)], and a hole velocity $v_h \sim 10^7$ cm/s.

We now turn to the implications of our results on the surface charge. The observed hole depletion and electron accumulation signifies a positively charged surface, suggesting the presence of empty, positively charged donor states. The change of the surface charge to negative under illumination with blue light requires the existence of empty surface acceptor states, which are persistently filled by photo-generated electrons. With red light, no persistent charging occurs, because the photo-generated electrons do not have enough energy to overcome the surface barrier of about 1.1 eV [7]. The observed electron accumulation even for the 6n17 sample means that surface donor states are still not filled with electrons, implying that these donor states must be located close to the conduction band - otherwise, they would be filled and neutral. The surface acceptor states, filled under blue illumination, must also be similarly high in energy as the surface donor states - otherwise, they would be filled as well at 6n17 doping, leading to a negative surface charge,

and thus changing the band bending to remove electron accumulation. For a cleaved Ge surface without oxide layer it is well established that Fermi level pinning exists close to the valence band, causing an upward band bending at the Ge surface with hole accumulation and electron depletion [32–35]. This is different to our commercial Ge wafers with a \sim nanometer-thin native oxide layer. The oxide can exist in various oxidation states GeO_x which may strongly affect the electronic properties/band bending of the Ge/ GeO_x interface [36, 37]. The prevailing oxidation state for native oxide is +4 (GeO_2), with the presence of GeO_x with $x < 4$ at the Ge/ GeO_2 interface [38]. Assuming that the band structure at the interface is determined by the band alignment of GeO_2 with a band gap of ~ 5.7 eV and a conduction band offset $\Delta E_c \sim 1$ eV with respect to Ge [39], we speculate that i), the band bending in Ge at the Ge/ GeO_2 interface is opposite to a cleaved Ge surface, yielding electron accumulation and hole depletion as illustrated for isotype heterojunctions in Ref. [1], and ii), the surface energy barrier is determined by ΔE_c . While the details of the Ge/ GeO_2 interface are important for device applications, its more detailed characterization is out of the scope of this study and remains for upcoming work. Here, our intention is to demonstrate the capability of charge carrier profiling in the near-surface region of a semiconductor which allows getting insights also in the surface characteristics.

VI. CONCLUSIONS

To the best of our knowledge this is the first time that by means of a contact-less, non-destructive local probe technique the free charge carrier concentration profile has been determined directly over a depth range from close to the surface up to 160 nm. We have shown by low-energy μSR that charge carrier profiles at semiconductor interfaces can be directly studied with nanometer depth resolution, if a muonium state forms in the semiconductor that is interacting with free carriers. The sensitivity of the technique depends on the cross section of carrier capture by the muonium state. In the case of Ge it is the interaction of the Mu_T^- state with holes at $T > 200$ K which is utilized for this purpose, where hole carrier concentrations can be determined in the range $10^{11} - 10^{15} \text{ cm}^{-3}$ by the measurable effect on the muon spin depolarization rate in transverse magnetic field. This allowed us to determine the hole carrier profile and its light induced manipulation in the hole depletion/electron accumulation region at the surface of commercial Ge wafers with a thin native GeO_2 layer on top.

As an outlook, the method can be applied to characterize on a microscopic level the properties of the GeO_x/Ge interface which might yield new insights for technologically relevant Ge device applications. The study of pre-cleaned surfaces, where the native oxide layer has been removed, would be interesting to provide complementary quantitative information on a nanometer scale of the ex-

pected hole accumulation due the Fermi level pinning close to the valence band.

ACKNOWLEDGMENTS

We gratefully acknowledge the help of P. Biswas and H. Luetkens in setting up the DOLLY and GPS experiments, and we thank H.P. Weber for his technical support in the operation of the LEM facility. The μSR measurements were performed at the Swiss Muon Source $S\mu\text{S}$, Paul Scherrer Institut, Villigen, Switzerland. The μSR data were analyzed using the program `musrfit` [41].

Appendix A: Ionization and hole capture rate parameters of the 1p15 sample

In Ref. [14] we used the p-type sample with $p \sim 10^{15} \text{ cm}^{-3}$ (1p15) to determine E_A , $\Lambda_c(200\text{K})$, and the exponent κ of the temperature dependence of Λ_c . Longitudinal field scan data at temperatures between 220 K and 290 K were fit with Eq. 2 with fixed $\Lambda_0 = 6.7 \cdot 10^{13}/\text{s}$ and fixed hyperfine coupling constant A_{hfc} of Mu_T^0 at its low temperature value of 2.36 GHz. Since A_{hfc} depends on temperature we re-analysed the data of Ref. [14] with a reduced $A_{hfc} = 2.15$ GHz in the temperature range 220 K – 290 K, and with a free Λ_0 parameter in the ionization rate $\Lambda_i(T)$. This procedure yields slightly different values of the ionization and hole capture rate parameters compared to Ref. [14]. These are $\Lambda_0 = 3.2(1.5) \cdot 10^{13}/\text{s}$, $E_A = 154(12) \text{ meV}$, $\Lambda_c(200\text{K}) = 2240(120) \cdot 10^6/\text{s}$, and exponent $\kappa = -2.2(2)$ of the temperature dependence of $\Lambda_c = \Lambda_c(200\text{K}) \cdot (T/200)^\kappa$.

Appendix B: Simulation of diamagnetic fractions

We use a simple model to calculate the diamagnetic fractions in Fig. 4. The fraction $x(E, [a : b])$ of muons with implantation energy E , stopping in a given depth interval $[a : b]$, is calculated using the simulated muon stopping profiles (see Fig. 2). For the slow component, $F_{D,S}$ is then given by

$$F_{D,S}(E, x[0 : b]) = x(E, [0 : b]) \cdot (0.8 - 0.3) + 0.3, \quad (\text{B1})$$

where we use the fact, that $F_D \sim 0.8$ at 220 K in the absence of holes, and $F_D \sim 0.3$ is the offset diamagnetic fraction, which does not originate from the thermally activated ionization of Mu_T^0 . Correspondingly, for the fast component $F_{D,F}$ in Fig. 4 b) we use

$$F_{D,F}(E, x[a : b]) = x(E, [a : b]) \cdot (0.8 - 0.3), \quad (\text{B2})$$

where $(0.8 - 0.3) = 0.5$ is the diamagnetic fraction of muons at 220 K originating from thermally activated ionization of Mu_T^0 , and which interact with holes.

Appendix C: Depolarization function of a sum of depth dependent exponential depolarization functions

The measured $\lambda_F = c \cdot p$, where c is a constant. In the case of a depth dependent $p(z)$ the depolarization rate will become a function of depth as well, $\lambda_F(z) = c \cdot p(z)$. This means that the depolarization function of an ensemble of muons with a stopping distribution $s(z)$ is an integral of exponentials weighted by $s(z)$. A sum of exponentials can be approximated by a stretched exponential function [40]. However, in our case the experimental data can be well fitted by a single exponential depolarization function. To test the validity of using a single exponential depolarization function, we added the μ SR data of energies {4,6,9,12,15,17,20} keV, where the average energy is 11.9 keV. The mean depth $\langle z \rangle$ of the sum of stopping dis-

tributions is 69.3 nm, which agrees well with the mean depth of the single 12 keV data with $\langle z \rangle = 67.5$ nm. The sum spectrum is very well fitted with an exponential depolarization function with a reduced χ^2 of 0.96 with 2036 degrees of freedom, strongly supporting the single exponential function model, where λ_F of the summed data agrees within statistical error with λ_F of the 12 keV single energy data. The same result is obtained when choosing a different set of data, e.g. {12,15,17,20} keV, where λ_F of the sum spectra with an average energy of 16 keV equals the λ_F of a single energy of 16 keV. This has the important implication that the measured λ_F , which is the average of λ_F 's across the muon stopping profile, reflects λ_F at the mean stopping depth, i.e. $\lambda_F = \lambda_F(\langle z \rangle)$. In other words, $\lambda_F(\langle z \rangle) = c \cdot p(\langle z \rangle)$, justifying the interpretation of the data, that the λ_F for a given muon implantation energy reflects the hole carrier concentration at the corresponding mean depth $\langle z \rangle$.

-
- [1] S. M. Sze and K. K. Ng, *Physics of Semiconductor Devices* (John Wiley & Sons, Inc., Hoboken, NJ, USA, 2006), 3rd ed.
- [2] D. K. Schroder, *Semiconductor Material and Device characterization* (John Wiley & Sons, Inc., Hoboken, NJ, USA, 2006), 3rd ed.
- [3] D. Ferry, *Semiconductors* (IOP Publishing Ltd, 2013).
- [4] B. D. Patterson, *Muonium States in Semiconductors*, Reviews of Modern Physics **60**, 69 (1988).
- [5] S. F. J. Cox, *Muonium as a Model for Interstitial Hydrogen in the Semiconducting and Semimetallic Elements*, Reports on Progress in Physics **72**, 116501 (2009).
- [6] A. Yaouanc and P. Dalmas de Réotier, *Muon Spin Rotation, Relaxation, and Resonance: Applications to Condensed Matter* (Oxford University Press, Oxford, UK, 2011).
- [7] T. Prokscha, K. H. Chow, E. Stilp, A. Suter, H. Luetkens, E. Morenzoni, G. J. Nieuwenhuys, Z. Salman, and R. Scheuermann, *Photo-Induced Persistent Inversion of Germanium in a 200-nm-deep Surface Region*, Scientific Reports **3**, 2569 (2013).
- [8] T. Prokscha, H. Luetkens, E. Morenzoni, G. J. Nieuwenhuys, A. Suter, M. Döbeli, M. Horisberger, and E. Pomjakushina, *Depth Dependence of the Ionization Energy of Shallow Hydrogen States in ZnO and CdS*, Physical Review B **90**, 235303 (2014).
- [9] E. Holzschuh, *Direct Measurement of Muonium Hyperfine Frequencies in Si and Ge*, Physical Review B **27**, 102 (1983).
- [10] R. L. Lichti, S. F. J. Cox, K. H. Chow, E. A. Davis, T. L. Estle, B. Hitti, E. Mytilineou, and C. Schwab, *Charge-State Transitions of Muonium in Germanium*, Physical Review B **60**, 1734 (1999).
- [11] I. Fan, K. H. Chow, B. Hitti, R. Scheuermann, A. I. Mansour, W. A. MacFarlane, B. E. Schultz, M. Egilmez, J. Jung, Y. G. Celebi, H. N. Bani-Salameh, B. R. Carroll, J. E. Vernon, and R. L. Lichti, *Influence of Photoexcitation on the Diamagnetic Muonium States in Ge Studied via their Precession Signatures*, et al., Physical Review B **78**, 153203 (2008).
- [12] D. G. Andrianov, G. G. Myasishcheva, Y. V. Obukhov, V. S. Roganov, G. I. Savelev, V. G. Firsov, and V. I. Fistul, *Interaction of Muonium with Atoms in the Crystal Lattice of Germanium*, Soviet Physics Semiconductors **12**, 92 (1978).
- [13] R. L. Lichti, K. H. Chow, and S. F. J. Cox, *Hydrogen Defect-Level Pinning in Semiconductors: The Muonium Equivalent*, Physical Review Letters **101**, 136403 (2008).
- [14] T. Prokscha, *Simulation of TF- μ SR Histograms in Germanium in the Presence of Cyclic Charge State Transitions of Muonium*, Journal of Physics: Conference Series **551**, 012049 (2014).
- [15] R. Kadono, R. M. Macrae, K. Nishiyama, and K. Nagamine, *Evidence for muonium passivation in n-doped Ge*, Physical Review B **55**, 4035 (1997).
- [16] T. Prokscha, *Monte-Carlo Simulation of Transitions between Different Muonium States*, Physics Procedia **30**, 50 (2012).
- [17] K. H. Chow, B. Hitti, R. F. Kiefl, S. R. Dunsiger, R. L. Lichti, and T. L. Estle, *Diffusion and Charge Dynamics of Negatively Charged Muonium in n-Type GaAs*, Physical Review Letters **76**, 3790 (1996).
- [18] K. H. Chow, R. F. Kiefl, J. W. Schneider, B. Hitti, T. L. Estle, R. L. Lichti, C. Schwab, R. C. DuVarney, S. R. Kreitzman, W. A. MacFarlane, et al., *Muonium Dynamics in Si at High Temperatures*, Physical Review B **47**, 16004 (1993).
- [19] T. Prokscha, E. Morenzoni, K. Deiters, F. Foroughi, D. George, R. Kobler, A. Suter, and V. Vrankovic, *The New μ E4 Beam at PSI: A Hybrid-Type Large Acceptance Channel for the Generation of a High Intensity Surface-Muon Beam*, Nuclear Instruments and Methods in Physics Research Section A **595**, 317 (2008).
- [20] W. Eckstein, *Computer Simulation of Ion-Solid Interactions* (Springer, Berlin, Heidelberg, New York, 1991).
- [21] E. Morenzoni, H. Glückler, T. Prokscha, R. Khasanov, H. Luetkens, M. Birke, E. M. Forgan, C. Niedermayer, and M. Pleines, *Implantation Studies of keV Positive Muons in Thin Metallic Layers*, Nuclear Instruments and Methods in Physics Research Section B **192**, 254 (2002).

- [22] E. Morenzoni, F. Kottmann, D. Maden, B. Matthias, M. Meyberg, T. Prokscha, T. Wutzke, and U. Zimmermann, *Generation of Very Slow Polarized Positive Muons*, *Physical Review Letters* **72**, 2793 (1994).
- [23] E. Morenzoni, H. Glckler, T. Prokscha, H. P. Weber, E. M. Forgan, T. J. Jackson, H. Luetkens, C. Niedermayer, M. Pleines, M. Birke, et al., *Low-Energy μ SR at PSI: Present and Future*, *Physica B: Condensed Matter* **289-290**, 653 (2000).
- [24] T. Prokscha, E. Morenzoni, C. David, A. Hofer, H. Glckler, and L. Scandella, *Moderator Gratings for the Generation of Epithermal Positive Muons*, *Applied Surface Science* **172**, 235 (2001).
- [25] T. Prokscha, K. H. Chow, H. Luetkens, E. Morenzoni, G. Nieuwenhuys, Z. Salman, R. Scheuermann, A. Suter, and H. P. Weber, *Low-Energy μ SR Investigations of Photo-Induced Effects on a nm Scale*, *Physics Procedia* **30**, 219 (2012).
- [26] E. Stilp, A. Suter, T. Prokscha, Z. Salman, E. Morenzoni, H. Keller, P. Pahlke, R. Hühne, C. Bernhard, R. Liang, et al., *Controlling the Near-Surface Superfluid Density in Underdoped $YBa_2Cu_3O_{6+x}$ by Photo-Illumination*, *Scientific Reports* **4** (2014).
- [27] A. Amato, H. Luetkens, K. Sedlak, A. Stoykov, R. Scheuermann, M. Elender, A. Raselli, and D. Graf, *The New Versatile General Purpose Surface-Muon Instrument (GPS) Based on Silicon Photomultipliers for μ SR Measurements on a Continuous-Wave Beam*, *Review of Scientific Instruments* **88**, 093301 (2017).
- [28] R. C. Vilão, R. B. L. Vieira, H. V. Alberto, J. M. Gil, and A. Weidinger, *Role of the transition state in muon implantation*, *Physical Review B* **96**, 195205 (2017).
- [29] R. C. Vilão, H. V. Alberto, J. M. Gil, and A. Weidinger, *Thermal spike in muon implantation*, *Physical Review B* **99**, 195206 (2019).
- [30] H. Lueth, *Solid Surfaces, Interfaces and Thin Films* (Springer, Berlin Heidelberg, 2010), 5th ed.
- [31] P. Y. Yu and M. Cardona, *Fundamentals of Semiconductors: Physics and Materials Properties* (Springer, Heidelberg Dordrecht London New York, 2010), 4th ed.
- [32] M. Kuzmin, P. Laukkanen, J. Makela, M. Tuominen, M. Yasir, J. Dahl, M. P. J. Punkkinen, and K. Kokko, *Origin of Fermi-level Pinning and its Control on the n-Type Ge(100) Surface*, *Physical Review B* **94**, 035421 (2016).
- [33] A. Dimoulas and P. Tsipas, *Germanium Surface and Interfaces (Invited Paper)*, *Microelectronic Engineering* **86**, 1577 (2009).
- [34] D. Kuzum, K. Martens, T. Krishnamohan, and K. C. Saraswat, *Characteristics of Surface States and Charge Neutrality Level in Ge*, *Applied Physics Letters* **95**, 252101 (2009).
- [35] G. W. Gobeli and F. G. Allen, *Photoelectric Properties and Work function of Cleaved Germanium Surfaces*, *Surface Science* **2**, 402 (1964).
- [36] D. Kuzum, T. Krishnamohan, A. J. Pethe, A. K. Okyay, Y. Oshima, Y. Sun, J. P. McVittie, P. A. Pianetta, P. C. McIntyre, and K. C. Saraswat, *Ge-Interface Engineering With Ozone Oxidation for Low Interface-State Density*, *IEEE Electron Device Letters* **29**, 328 (2008).
- [37] D. Schmeisser, R. D. Schnell, A. Bogen, F. J. Himpsel, D. Rieger, G. Landgren, and J. F. Morar, *Surface Oxidation States of Germanium*, *Surface Science* **172**, 455 (1986).
- [38] S. K. Sahari, H. Murakami, T. Fujioka, T. Bando, A. Ohta, K. Makihara, S. Higashi, and S. Miyazaki, *Native Oxidation Growth on Ge(111) and (100) Surfaces*, *Japanese Journal of Applied Physics* **50**, 04DA12 (2011).
- [39] A. Ohta, H. Nakagawa, H. Murakami, S. Higashi, and S. Miyazaki, *Photoemission Study of Ultrathin GeO_2/Ge Heterostructures Formed by UV- O_3 Oxidation*, *e-Journal of Surface Science and Nanotechnology* **4**, 174 (2006).
- [40] D. C. Johnston, *Stretched Exponential Relaxation Arising from a Continuous Sum of Exponential Decays*, *Physical Review B* **74**, 184430 (2006).
- [41] A. Suter and B. M. Wojek, *Musrfit: A free platform-independent framework for μ SR data analysis*, *Physics Procedia* **30**, 69 (2012).